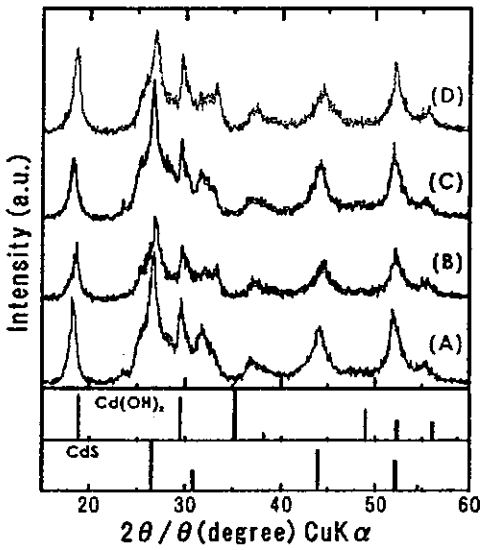

Fig.4 XRD patterns of CdS/MWCNTs

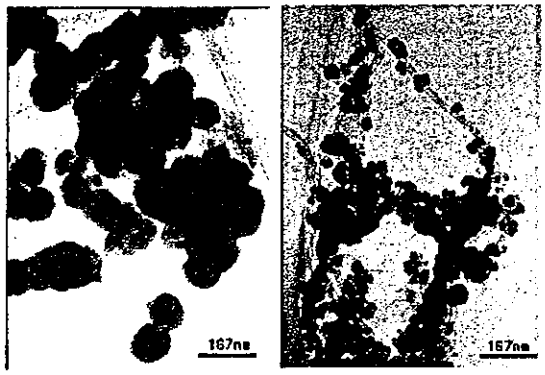

Fig.5 TEM images of CdS/MWCNTs
left;(B), right;(C)

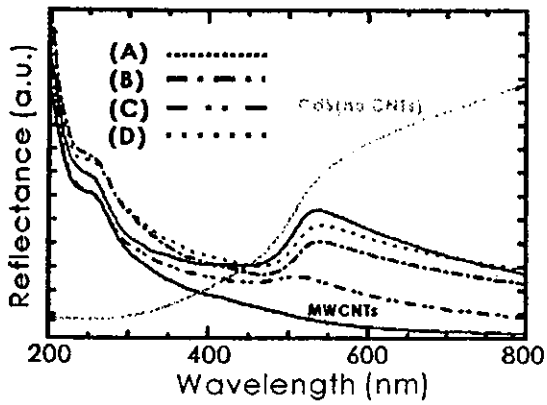

Fig.6 UV-VIS spectra of CdS/MWCNTs

samples (A)-(D) are shown in Fig. 6. Though the absorption edge of all the samples appeared around 500 nm, the reflection coefficients of the samples varied. This may be due to the variation in particle morphology. In the case of CdS deposited on a rough glass surface by CBD method, the particle size becomes smaller[7]. If we compare the nanotube surfaces, sample B and C has smooth and rough textures respectively. And also, the size of the particles deposited on sample B and C were large and small respectively. This was in agreement with what was observed in the case of CdS deposited on rough glass surface. It is inferred that the difference in particle size is due to the difference in free energy change during nucleation caused by the surface morphology of the nanotubes.

3.3 Photoreactivity of CdS/MWCNTs

Fig.7 shows the results of hydrogen generation experiment carried out using the CdS/MWCNTs photocatalyst dispersed in Na_2S solution and exposed to visible light irradiation. The results include that of CdS without MWCNTs as a control. It was obvious that the use of MWCNTs as a substrate had an effect on the photocatalytic activities of CdS. Among the samples tested, highest activity was reported for the sample B. The poor activities of other samples were considered due to the difference in the crystallinity of the MWCNTs. In the case of sample A, the surface was not free of defects. On the other hand, in the case of sample C, the surface was full of defects. Though the sample D was annealed to reduce the number of defects on the surface, the photoactivity was not enhanced enough compared with sample B. However, activity of sample D was higher than that of C and almost equal to A. Considering the above facts, we believe that the photocatalytic activity is closely related to the crystallinity of the MWCNTs. The reason being that the electronic property of the MWCNTs depends very much on the crystallinity[8]. Thus the electron transport property (which is the key issue in photocatalysis) have been enhanced in highly crystalline MWCNTs. MWCNTs supposed to play a role similar to that of platinum on platinum supported CdS and also helps to separate the oxidation-reduction reaction sites for promoting photocatalytic activities by preventing recombination of photo excited electrons and holes.

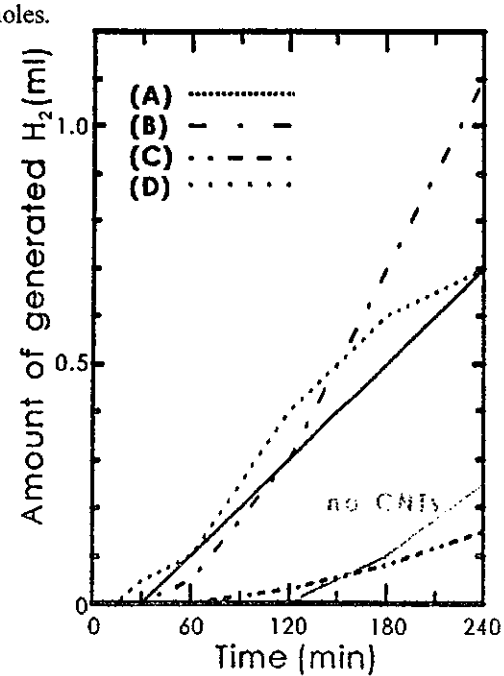

Fig.7 Amount of generated hydrogen

4. CONCLUSION

CdS was deposited on the surface modified MWCNTs by CBD method. The deposited particle sizes become smaller with increasing defects. The results of hydrogen generation experiment suggested that photocatalytic activities were dependent on the crystallinity of MWCNTs rather than CdS particle size. As the electric property is linked to the crystallinity of the nanotubes, it is assumed that photo excited electrons are easily transferred from CdS to MWCNTs and moved to reaction sites. In other words, it is predicted that the MWCNTs act as a metal catalyst such as Pt that causes site separation effect.

5. REFERENCE

[1]T.Arai, S.Sakima, Y.Sato, K.Shinoda, B.Jeyadevan and K.Tohji
Shigen-to-Sozai, **119**, 713-720 (2003)
[2]S.Iijima, *Nature*, **354**, 56 (1991)
[3]S.F.McKay, *J.Appl.Phys.*, 1964, **35**, (1992)
[4]J.Liu *et al.*,*Science*, 1253,**280**,(1998)
[5]Yan-Hui.Li, Shuguang.Wang, Zhaokun Luan, Jun Ding, Cailu Xu and Dhai Wu,
Carbon, **41**, 1057-1062 (2003)
[6]A.M.Zhang, J.L.Dong, Q.H.Xu, H.K.Rhee and X.L.Li,
Catalysis Today, **93-95**, 347-352 (2004)
[7]T.Yakubo, Master's thesis (2002)
[8]J.C.Charlier, *Acc. Chem. Res.* , **35**, 1063-1069 (2002)

Available online at www.sciencedirect.com
SCIENCE DIRECT®
ELSEVIER
Journal of Magnetism and Magnetic Materials 282 (2004) 122–126
Journal of magnetism and magnetic materials
www.elsevier.com/locate/jmmm

Crystallographic structures and magnetic properties of $L1_0$-type FePt nanoparticle monolayered films stabilized on functionalized surfaces

Y. Sasaki[a,*], M. Mizuno[a], Andrew C.C. Yu[a], M. Inoue[a], K. Yazawa[a], I. Ohta[b], M. Takahashi[b], B. Jeyadevan[c], K. Tohji[c]

[a] *Sony Corporation Sendai Technology Center, Tagajo, Miyagi 985-0842, Japan*
[b] *Department of Electric Engineering, Tohoku University, Aoba-ku, Sendai 980-8579, Japan*
[c] *Graduate School of Environmental Studies, Tohoku University, Aoba-ku, Sendai 980-8579, Japan*

Available online 10 May 2004

Abstract

Crystallographic structures and magnetic properties of chemically synthesized FePt nanoparticles, which were firmly stabilized into a monolayer on thermally oxidized Si substrate using 3-amino propyldimethylethoxysilene, were studied. The two-dimensional structure of FePt nanoparticles was confirmed by plan-view high-resolution scanning microscopy observation. The particles transformed from fcc to highly ordered $L1_0$ structure by annealing at 800°C under high vacuum with minimal coalescence. From rotational hysteresis loss analysis, a large magnetic anisotropy field of over 80 kOe for the 800°C-annealed film was estimated. The coercivity of the annealed sample was very small and of the order of 10^2 Oe at room temperature, meanwhile, the remanence coercivity obtained from DC demagnetization measurement was over 11 kOe. This large difference was resulted from the co-existence of Fe-poor particles with different low anisotropy fields in the monolayered film.

PACS: 75.50.Tt; 75.75.+a; 75.50.Ss

Keywords: FePt nanoparticle; $L1_0$ phase; Monolayered film; Coupling layer; Coalescence; Coercivity; Magnetic anisotropy field

1. Introduction

There have been increasing demands for ultra-high density recording in magnetic storage media. $L1_0$ type alloys such as FePt and CoPt have great potential as the promising candidate because of their high magnetocrystalline anisotropy ($K_u \sim 6.6 \times 10^7$ erg/cm^3) [1]. Recently, many successful results regarding chemical syntheses of FePt and CoPt nanoparticles in solution phase have been reported [2–8]. Chemically synthesized FePt nanoparticles have fine size of a few nm with narrow size distribution and can be easily constructed to well-aligned microstructure, which

*Corresponding author. Tel.: +81-22-367-2727; fax: +81-22-367-2725.
E-mail address: yuichi.sasaki@jp.sony.com (Y. Sasaki).

0304-8853/$ - see front matter © 2004 Elsevier B.V. All rights reserved.
doi:10.1016/j.jmmm.2004.04.029

allows for realization of recording densities over 1 Tb/in^2. As-grown FePt nanoparticles are mostly face-centered cubic (fcc) with chemically disordered phase and show superparamagnetic behavior. High-temperature annealing is therefore required to obtain the high anisotropy ordered $L1_0$ phase. Self-organized deposition is one of the effective techniques for forming nanoparticles on a substrate into mono- or multi-layer, however, those in the resulting array tend to coalesce during annealing [9,10], which leads to undesirable exchange interaction between particles as well as increase in size distribution. We recently demonstrated the application of using amino-functional silane, 3-(2-aminoethlyamino) propyltrimethoxysilane, as a coupling layer for FePt nanoparticles dispersion, resulting in the formation of monolayered film on rigid substrates [11]. Coalescence of the nanoparticles was not significant after annealing at 800°C. This fabrication method also enabled nanoparticles to stabilize homogeneously compared to the self-organized procedure over an extended area. In this paper, magnetic properties of FePt nanoparticle monolayered films which were prepared by employing a coupling layer described above as well as crystal structure analysis of the particles are described.

2. Experiment

FePt nanoparticles were produced based on the method reported by Sun et al. [2]. As an attempt to control the chemical composition distribution, the reaction were performed without 1, 2-hexadecanediol to reduce Pt(II). Our recent results have shown that the distribution in the composition of nanoparticles was reduced by the method without such a diol [12]. In case of the absence of a diol, CO-ligand released from iron pentacarbonyl works as a reducing agent [13], which allows us to obtain the alloy nanoparticles. The heterostructure of FePt nanoparticles monolayered films with the 3-amino propyldimethylethoxysilene (APS) coupling layer was fabricated by the similar method reported in Ref. [11]. Initially, deposited FePt nanoparticle monolayered films were annealed under a vacuum of 10^{-7} Torr at temperatures of 600°C and 800°C for 30 min in order to transform the FePt nanoparticles from the fcc to the $L1_0$ phase.

The average crystallographic textures and grain sizes of the FePt nanoparticle monolayered films were investigated by in-plane X-ray diffraction (XRD) measurements with the X-ray incidence angle set at 0.25° from the plane. The in-plane XRD measurements were done using a RIGAKU ATX-G with Cu-K_α (wavelength = 0.154184 nm) radiation. Further characterizations of the particle sizes and surface morphology of the film were carried out using high-resolution scanning electron microscopy (HR-SEM) and high-resolution transmission electron microscopy (HR-TEM). Chemical compositions were determined by X-ray microanalysis (XMA) for measuring FePt nanoparticle assembly and electron dispersive X-ray spectroscopy equipped on TEM (TEM-EDS) for charactering less than 10 FePt nanoparticles per measurement. Magnetic measurements were performed using superconducting quantum interference device (SQUID) magnetometer and high-sensitivity torque magnetometer.

3. Morphology, chemical composition and crystallographic structures

Fig. 1 shows the HR-TEM image of as-prepared FePt nanoparticles. Most particles were found to be single crystals, meanwhile, faceted morphology was also observed. Core-shell structure between Fe and Pt was not observed. The mean diameter of the particles was 4.2 nm with a standard deviation

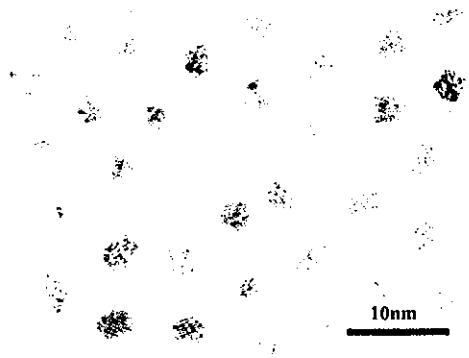

Fig. 1. HR-TEM image of as-prepared FePt nanoparticles.

Table 1
Chemical composition analyzed by XMA and TEM-EDS

	The number of measured particles	Fe(at%)	Pt (at%)
XMA	$>10^6$	48	52
TEM-EDS	<10	47.67	52.33
		44.29	55.71
		43.78	56.22
		38.79	61.21
		30.59	69.41

of 0.46 nm (11%). Chemical composition data of FePt nanoparticles analyzed by two methods, named XMA and TEM-EDS are shown in Table 1. The XMA data, which was obtained by measuring over 10^6 particles, corresponded to the average composition. Meanwhile, we collected the composition data from 1–10 particles at TEM-EDS measurements by narrowing the electron beam size, allowing us to know the composition distribution of approximately each particle. Average composition of this sample was $Fe_{48}Pt_{52}$, however, we found the inhomogeneity of the composition according to the TEM-EDS results. $L1_0$ phase is thermodynamically equilibrium structure of Fe_xPt_{100-x} alloy system in the range of $45 \leqslant x \leqslant 65$ [14]. EDS data suggested that a significant number of particles were out of this range. EDS data also showed relatively small values of Fe content in numerous particles compared to the XMA overall result [12].

A plan-view image of the nanoparticles observed using an HR-SEM is shown in Fig. 2. The particles were stabilized randomly in a two-dimensional pattern with an ideal separation of a few nm. The particle coverage on the substrate had a high density of approximately 6.4 T particles/in^2. For further characterization of the APS/FePt nanoparticle heterostructure, X-ray reflectivity measurements were carried out. According to the simulation using multilayer model [15], monolayered structure of FePt nanoparticle films over an extended area ($1 \times 3\,cm^2$) was confirmed.

The average crystallographic structure of FePt nanoparticle monolayered films were determined using in-plane XRD. Fig. 3 shows the in-plane XRD patterns for as-deposited and annealed FePt

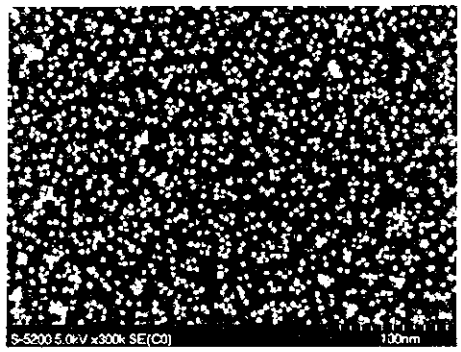

Fig. 2. Plan-view HR-SEM image of the FePt nanoparticle film. Bright dots correspond to the nanoparticles.

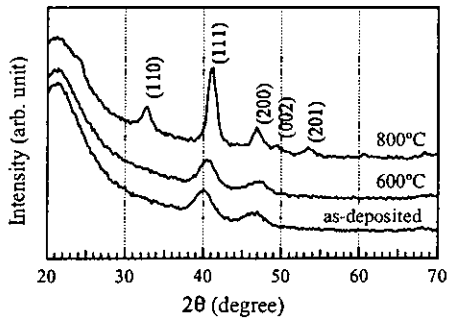

Fig. 3. In-plane XRD patterns for the as-deposited and annealed FePt nanoparticle monolayered films.

nanoparticle monolayered films. The chemically disordered fcc (1 1 1) and (2 0 0) peaks appeared at the as-deposited film. After annealing the film at 600°C for 30 min under a vacuum of 10^{-7} Torr, these two peaks shifted to higher angles. In addition, the annealed film at higher temperature of 800°C for 30 min under the same vacuum allowed us to observe a chemically ordered $L1_0$ (1 1 0) superlattice reflection as well as the (2 0 0)/(0 0 2) splitting. The *c/a* ratio, calculated using the (1 1 1) and (2 0 0) peaks, of the film annealed at 600°C was almost unity, meaning that transformation into $L1_0$ phase did not occur. Conversely, the *c/a* ratio for the film annealed at 800°C was determined to be 0.954, which was comparable to that of the bulk data of 0.964 [16]. Thus, the 800°C-annealed film was considered to have a highly ordered $L1_0$ phase. Grain diameters of the nanoparticles, which was calculated by the

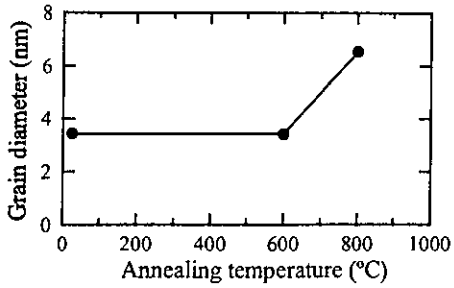

Fig. 4. Grain diameter of the as-deposited FePt nanoparticle monolayered film and the films prepared by annealing, estimated by Scherrer's equation using (1 1 1) peaks.

Scherrer's equation using the full-width at half-maximum of the (1 1 1) peak, are plotted in Fig. 4. There was no change in diameter after annealing at 600°C, suggesting that coalescence was avoided during annealing. On the other hand, the diameter after annealing at 800°C increased approximately 100%. However, the degree of coalescence for the FePt nanoparticles array with a highly ordered $L1_0$ phase was not significant compared to the other study [5].

4. Magnetic properties

Fig. 5 shows in-plane hysteresis loops of the as-deposited and the annealed FePt naonoparticle films which were measured at (a) room temperature (RT) and (b) 5 K, respectively. The as-deposited and 600°C-annealed films exhibited superparamagnetic behavior at room temperature, which was consistent with the fact that their crystallographic structure revealed chemically disordered fcc phase with low magnetic anisotropy. The magnetization curves of the nanoparticle film annealed at 800°C drew the loops with complicated shapes. Especially, the coercivity was of the order of 10^2 Oe at RT even though XRD results demonstrated the transformation into high magnetic anisotropy ordered $L1_0$ phase. To make the reason clear, the remanence coercivity (H_{cr}) and the magnitude of uniaxial magnetic anisotropy field (H_k) was evaluated in the film plane. DC demagnetization curve measured with a saturation field of 50 kOe for the film annealed at 800°C is

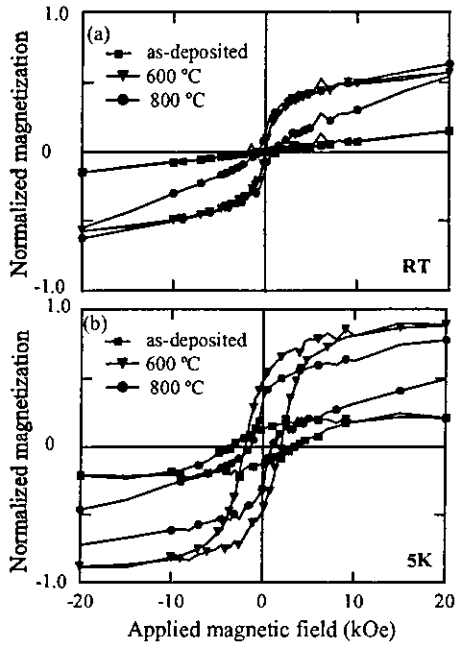

Fig. 5. In-plane hysteresis loops of the as-deposited FePt nanoparticle monolayered film and the annealed films measured at (a) room temperature (RT) and (b) 5 K.

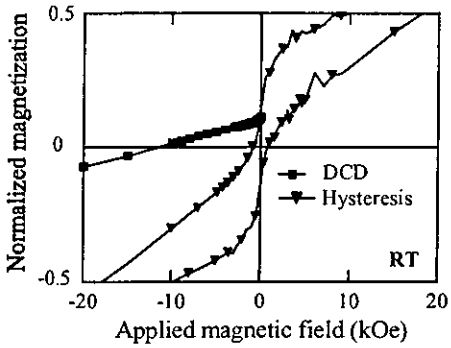

Fig. 6. DC demagnetization (DCD) and hysteresis curves for FePt nanoparticle films annealed at 800°C.

shown in Fig. 6. The large H_{cr} of over 11 kOe for the 800°C-annealed film was observed, and then the extremely large H_{cr}/H_c value (=14.21) was demonstrated compared to the theoretical value of 1.07 [17]. These results suggest that at least 2 phases with different anisotropies existed in the film. Rotational hysteresis loss (W_r) for the 800°C-annealed film is plotted as a function of

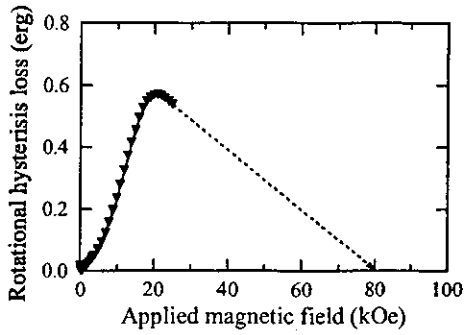

Fig. 7. Rotational hystersis loss curve for the 800°C-annealed film. The dotted arrow indicates the estimated H_k value.

the applied field up to 25 kOe in Fig. 7. W_r measurement was employed to estimate the intrinsic H_k of each grain [18]. H_k of each grain is generally determined as the magnetic field where W_r become zero at a higher field. In the case of the 800°C-annealed film, W_r kept high value at upper limit of the applied field for the measurement. We, therefore, estimated the approximate H_k value by extrapolating the decreasing part of W_r curve to $W_r = 0$. As can be seen in Fig. 7, it is suggested that the particles in the film had a very large H_k of more than 80 kOe. A possible explanation against these inconsistencies is the co-existence of Fe-poor particles which could not transform into $L1_0$ structure. These particles were likely remained at their fcc structure or transformed $FePt_3$ structure with low magnetic anisotropy after the thermal treatment, therefore, the superparamagnetic characteristics of the particles was obtained. If the $FePt_3$ particles were involved in the whole particle film with insignificant amount, the clear evidence would be invisible on XRD pattern.

5. Conclusions

Chemically synthesized FePt nanoparticle monolayer can be firmly stabilized on an amino-functionalized surface. The FePt nanoparticles transformed from fcc to highly ordered $L1_0$ structure by annealing at 800°C under high vacuum with minimal coalescence. It was estimated that the 800°C-annealed film had a large magnetic anisotropy field of more than 80 kOe. In addition, remanence coercivity for the film annealed at 800°C revealed over 11 kOe. However, the coercivity indicated very small value of the order of 10^2 Oe at room temperature, which suggested the existence of low anisotropy components. This is expected to be due to incomplete $L1_0$ phase transformation of the Fe-poor particles. The investigation of narrowing the chemical composition distribution of FePt nanoparticles is in active progress.

References

[1] D. Weller, A. Moser, IEEE Trans. Magn. 35 (1999) 4423.
[2] S. Sun, C.B. Murray, D. Weller, L. Folks, A. Moser, Science 287 (2000) 1989.
[3] S. Sun, E.E. Fullerton, D. Weller, C.B. Murray, IEEE Trans. Magn. 37 (4) (2001) 1239.
[4] A.C.C. Yu, M. Mizuno, Y. Sasaki, H. Kondo, K. Hiraga, Appl. Phys. Lett. 81 (2002) 3768.
[5] S. Sun, S. Anders, T. Thomson, J.E.E. Baglin, M.F. Toney, H.F. Hamann, C.B. Murray, B.D. Terris, J. Phys. Chem. B 107 (23) (2003) 5419.
[6] M. Chen, D.E. Nikles, Nano Lett. 2 (3) (2002) 211.
[7] M. Chen, D.E. Nikles, J. Appl. Phys. 91 (10) (2002) 8477.
[8] B. Jeyadevan, K. Urakawa, A. Hobo, N. Chinnasamy, K. Shinoda, K. Tohji, D.D.J. Djayaprawira, M. Tsunoda, M. Takahashi, Jpn. J. Appl. Phys. 42 (2003) L350.
[9] Z.R. Dal, S. Sun, Z.L. Wang, Nano Lett. 1 (8) (2001) 443.
[10] S. Wang, S.S. Kang, D.E. Nikles, J.W. Harrell, X.W. Wu, J. Magn. Magn. Mater. 266 (2003) 49.
[11] A.C.C. Yu, M. Mizuno, Y. Sasaki, M. Inoue, H. Kondo, I. Ohta, D. Djayaprawira, M. Takahashi, Appl. Phys. Lett. 82 (2003) 4532.
[12] A.C.C. Yu, M. Mizuno, Y. Sasaki, Appl. Phys. Lett., to be submitted.
[13] E.V. Shevchenko, D.V. Talapin, H. Schnablegger, A. Kornowski, Ö. Festin, P. Svedlindh, M. Haase, H. Weller, J. Am. Chem. Soc. 125 (2003) 11480.
[14] T.B. Massalski, H. Okamoto, P.R. Subramanian, L. Kacprzak, Binary Alloy Phase Diagrams, ASM International, Materials Park, OH, 1990.
[15] J. Daillant, A. Gibaud, X-ray and Neutron Reflectivity: principles and applications, Springer, New York, 1999.
[16] JCPDS-International Centre for diffraction Data, 1999.
[17] E.P. Wolfarth, J. Appl. Phys. 29 (1958) 595.
[18] M. Takahashi, T. Shimatsu, M. Suekane, M. Miyamura, K. Yamaguchi, H. Yamasaki, IEEE Trans. Magn. 28 (5) (1992) 3285.

X-ray Absorption Fine Structure Studies on the Local Structures of Ni Impurities in a Carbon Nanotube

Kiyotaka Asakura,[†] Wang-Jae Chun,[†,††] Kazuyuki Tohji,[†††] Yoshinori Sato,[†††] and Fumio Watari[††††]

[†]*Catalysis Research Center, Hokkaido University, Sapporo, Hokkaido 001-0021*

[††]*Core Research for Evolutional Science and Technology, Japan Science and Technology Corporation, Sapporo, Hokkaido 001-0021*

[†††]*Graduate School of Environmental Studies, Tohoku University, Aoba, Sendai, 980-8579*

[††††]*Graduate School of Dental Medicine, Department of Biomedical, Dental Materials & Engineering, Hokkaido University, Kita 13 Nishi 7 Sapporo, Hokkaido 060-8586*

(Received October 21, 2004; CL-041243)

Local structure around Ni impurities in a carbon nanotube was studied by X-ray absorption fine structure (XAFS). The Ni was present in the form of Ni particles before the purification process. After the purification Ni content was decreased to a few hundreds ppm. The Ni K-edge XAFS could be measured by a 19 element solid-state detector. The Ni species was strongly bound to the carbon of the carbon nanotube with a Ni–C covalent bonds at 0.173 nm.

Carbon nanotubes draw much attention as new materials, which have wide applications to many fields such as electric devices, hydrogen storage materials, field emission display, AFM tip, and so on.[1] Since carbon nanotubes are composed of only carbon atoms and are expected to have biocompatibility, the researches for the biological application have been started such as a drag delivery system, scaffolds for cell engineering, artificial bones, dental roots, and cell culture media.[2] Chemical vapor deposition (CVD) synthesis method using catalysts such as Ni, Fe, Fe–Ni, and Ni–Mo is one of promising methods for large-scale production of carbon nanotubes.[3] Ni is one of the best catalysts to produce carbon nanotubes but it often shows toxic properties to a living body. Although most of Ni in the carbon nanotube can be removed by the HCl treatment, it is important to know the metabolism, chemical state, and structure of Ni impurity left in the carbon nanotubes after the HCl treatment in order to apply the nanotubes to medical and biological fields safely. In this paper, we report the characterization of the chemical state of residual Ni species before and after the purification processes of a carbon nanotube by XAFS (X-ray absorption fine structure) technique. Because the amount of Ni species after the purification is about a few hundred ppm, it is difficult to estimate the Ni chemical state by conventional techniques. We carried out fluorescence XAFS analysis of Ni impurity in the carbon nanotube. We found that the Ni species was strongly fixed to the carbon of a carbon nanotube through a Ni–C covalent bond.

Carbon nanotube was synthesized by a CVD method using Ni catalyst. It was purified by a calcination followed by 6 M HCl treatment for 6 h in order to remove the carbon nanoparticles and Ni catalysts.

XAFS measurements were carried out at BL9A of the Photon Factory in Institute for Structure Material Science (KEK-PF) using a Si(111) double crystal monochromator.[4] (99G280, 2001G287) The incident and transmitted X-rays were monitored by ionization chambers filled with nitrogen. The fluorescence X-ray was detected by a 19 element SSD (solid state detector) (Camberra Co.) The dead times of SSD were corrected according to the literature.[5] The XAFS analyses were carried out by REX2000 (Rigaku Co) using phase shift and amplitude functions derived from FEFF8.[6,7]

Figure 1 showed the Fourier transforms of Ni K-edge XAFS oscillations before the purification over $k = 30$–$150\,\mathrm{nm}^{-1}$. We measured the XAFS oscillation in a transmission mode because we had an enough edge jump. We found several peaks. The first and main peak appeared at 0.25 nm, which corresponded to that of the Ni–Ni distance in the first shell of Ni metal. The longer Ni–Ni peaks clearly appeared, which were corresponding to the 2nd, 3rd and 4th shells in the Ni fcc structure. The curve fitting analysis showed that the coordination number and bond distance of the first shell Ni–Ni bond were 12 and 0.248 nm, respectively, indicating that the Ni was present in a metal particle larger than 5 nm judging from the coordination numbers of the first and the higher shells which were almost equal to that of the bulk Ni species.[8]

When the Ni metal particles were removed by the HCl treatment, we could not observe Ni K-edge in a transmission mode any more. Thus we used a fluorescence mode to obtain Ni XAFS oscillations. According to the Ni Kα fluorescence peak intensity, the amount of Ni can be estimated to be about a few hundred ppm. Figure 2 shows the X-ray near edge structure of Ni species in the carbon nanotube before and after the HCl treatment to-

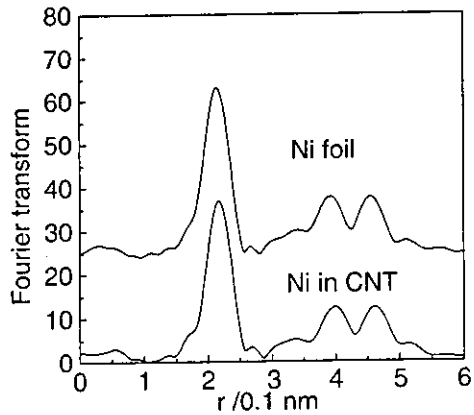

Figure 1. Fourier transforms of XAFS oscillations for Ni catalysts in the carbon nanotube and Ni foils.

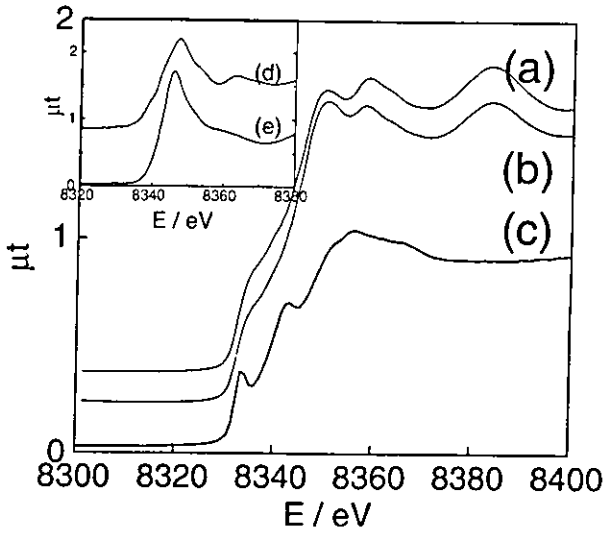

Figure 2. Ni K-edge XANES of (a) Ni foil, (b) Ni species in the carbon nanotube before purification, and (c) that after the purification. (d) and (e) in the inset showed XANES spectra for NiO and $Ni(NO_3)_2 \cdot 9H_2O$.

gether with reference compounds. The XANES (X-ray absorption near edge structure) spectrum after the HCl treatment was completely different from that before the HCl treatment and Ni foil, indicating that the metallic Ni particles were completely removed by the HCl treatment. The XANES spectrum of the sample after the HCl treatment was different from those of NiO and $Ni(NO_3)_3 \cdot 9H_2O$. The residual Ni species was not simple oxide or aquo complex ions. Peaks in the XANES spectrum appeared at the similar positions as in the spectrum of the deactivated Ni catalyst after the CH_4 decomposition reaction though the peak heights were much stronger in the present spectrum.[9]

Figure 3 shows the Fourier transforms of Ni K-edge XAFS of Ni species in the carbon nanotube after the HCl treatment. Peaks appear at 0.16 and 0.22 nm. We carried out curve fitting analysis for the first shell assuming Ni–C bond. The bond distance and coordination number were 0.177 nm and 1.5, respectively. The second shell peak could be assigned to Ni–Ni at 0.247 nm with its coordination number 0.8. Ni–C distance 0.177 nm was smaller than 0.186 and 0.184 nm found in Ni_3C and $Ni(CO)_4$, respectively. Thus the Ni species was fixed strongly to carbon nanotube through a covalent bond. Since carbon nanotubes were stable in the living body, Ni impurity may stay there for a long time and may bioaccumulate. We recommend that the Ni catalyst should not be used to the production of the carbon tube if it is used as a biomaterial.

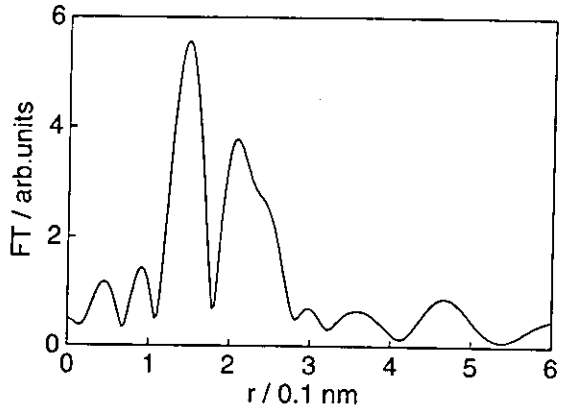

Figure 3. Fourier transform of Ni K-edge EXAFS for the Ni species in the carbon nanotube after the HCl treatment.

References

1 P. J. F. Harris, "Carbon Nanotubes and Related Structures: New Materials for the Twenty-first Century," Cambridge University Press, Cambridge (1999).
2 "Nanotoxicology and Development of Carbon Nanotubes and Nano/Micro Particles for Biomedical Applications," ed. by F. Watari, Springer Verlag, Berling, to be published.
3 M. Endo, Y. A. Kim, T. Hayashi, T. Yanagisawa, H. Muramatsu, M. Ezaka, H. Terrones, M. Terrones, and M. S. Dresselhaus, *Carbon*, **41**, 1941 (2003).
4 M. Nomura, *KEK Report*, **98-194**, 1 (1998).
5 M. Nomura,*KEK Report*, **98-4**, 1 (1998).
6 K. Asakura, "X-ray Absorption Fine Structure for Catalysts and Surfaces," ed. by Y. Iwasawa, World Scientific, Singapore (1996), pp 33–58.
7 S. I. Zabinsky, J. J. Rehr, A. Ankudinov, R. C. Albers, and M. J. Eller, *Phys. Rev. B*, **52**, 2995 (1995).
8 R. B. Greegor and F. W. Lytle, *J. Catal.*, **63**, 476 (1980).
9 S. Takenaka, H. Ogihara, and K. Otsuka, *J. Catal.*, **208**, 54 (2002).

Published on the web (Advance View) February 12, 2005; DOI 10.1246/cl.2005.382

Available online at www.sciencedirect.com
SCIENCE DIRECT®
ELSEVIER
Journal of Magnetism and Magnetic Materials 288 (2005) 470–477
Journal of magnetism and magnetic materials
www.elsevier.com/locate/jmmm

Effect of zinc substitution on Co–Zn and Mn–Zn ferrite nanoparticles prepared by co-precipitation

R. Arulmurugan[a,*], B. Jeyadevan[b], G. Vaidyanathan[a], S. Sendhilnathan[c]

[a]*Department of Physics, Pondicherry Engineering College, Pondicherry 605014 India*
[b]*Graduate School of Environmental Studies, Tohoku University, Sendai 980-8579, Japan*
[c]*Department of Physics, Sri Manakula Vinayagar Engineering College, Pondicherry 605 107 India*

Received 10 July 2004; received in revised form 29 September 2004
Available online 10 November 2004

Abstract

$Co_{(1-x)}Zn_xFe_2O_4$ and $Mn_{(1-x)}Zn_xFe_2O_4$ ($x = 0.1-0.5$) nanoparticles less than 12 nm are prepared by chemical co-precipitation method which could be used for ferrofluid preparation. X-ray diffraction (XRD), Transmission electron microscopy (TEM), Vibrational sample magnetometer (VSM) and Thermo gravimetric analysis (TGA) are utilized in order to study the effect of variation in the Zn substitution and its impact on particle size, magnetic properties like M_S, H_C, Curie temperature, thermomagnetic coefficient and associated water content. Atomic absorption spectroscopy was used for the estimation of cobalt, zinc and manganese and Fe^{3+} ion was estimated using spectrophotometer. The saturation magnetization of the Co–Zn substituted ferrite nanoparticles decreases continuously with the increase in Zn concentration, whereas for the Mn–Zn substituted ferrite nanoparticle the saturation magnetization was maximum for $x = 0.2$ and decreases on further increase in Zn concentration. The particle size decreases with the increase in the Zn concentration for both Co–Zn and Mn–Zn ferrites. The estimation of associated water content, which increases with the Zn concentration, plays a vital role for the correct determination of cation contents. The Curie temperature and the temperature at which maximum value of thermomagnetic coefficient observed simultaneously decrease with the increase in the initial substitution degree of zinc.

PACS: 75.50.Mm; 75.50.Tt; 75.75.+a; 75.47.Pq

Keywords: Chemical co-precipitation method; Thermomagnetic coefficient; Co–Zn ferrites; Mn–Zn ferrites; Nanoferrites

1. Introduction

Magnetic nanoparticles are of great technological importance because of their use in magnetic fluid, information storage system, medical

*Corresponding author. Tel.: +91 413 2655281x641; fax: +91 413 2655101.
E-mail addresses: arulphysics@rediffmail.com (R. Arulmurugan), gvn_pec@yahoo.com (G. Vaidyanathan).

0304-8853/$ - see front matter © 2004 Elsevier B.V. All rights reserved.
doi:10.1016/j.jmmm.2004.09.138

diagnostics, etc. Various preparation techniques have been used for the synthesis of fine particles of ferrites, which exhibit novel properties when compared to their properties in bulk. Non-conventional methods such as co-precipitation, thermal decomposition, sol–gel and hydrothermal methods have been widely used. Ultra fine ferrite particles can be prepared by the simple chemical co-precipitation method. Auzans et al. [1,2] have studied the preparation and properties of Mn–Zn ferrite nanoparticles used for ionic and surfacted ferrofluids with different degrees of Zn substitution prepared by co-precipitation method. Chandana Rath et al. [3] have reported the dependence on cation distribution of particle size, lattice parameter and magnetic properties in nanosize Mn–Zn ferrite for different degrees of Zn substitution prepared by hydrothermal precipitation method. The use of Mn–Zn ferrite for the preparation of temperature sensitive magnetic fluid by co-precipitation method has already been studied [4–6]. $Co_{0.2}Zn_{0.8}Fe_2O_4$ fine particles have been prepared by chemical co-precipitation method followed by sintering [7]. Control of particle size in the nanometer range by the variation of synthesis condition is always a difficult task. It becomes mandatory in the case of ferrofluid preparation using co-precipitation method. In order to prepare ferrofluid having such fine particles, specific size restriction is imposed considering the stability criteria. $Co_{(1-x)}Zn_xFe_2O_4$ substituted ferrites with x varying from 0.1 to 0.5 prepared by co-precipitation method have not yet been fully studied like Mn–Zn substituted ferrites. In this paper we report preparation of $Me_{1-x}Zn_xFe_2O_4$ fine particles, where $Me = Co^{2+}$ and Mn^{2+} with x varying from 0.1 to 0.5 with particle size less than 12 nm by chemical co-precipitation method and the consequent change in their magnetic property, thermomagnetic coefficient, lattice parameter, particle size and associated water content due to zinc substitution. Though further increase in the Zn concentration ($x > 0.5$) leads to the formation of ferrite nanoparticles, because of the low-magnetic volume force when dispersed in a carrier liquid, particles with $x > 0.5$ are not considered.

2. Experimental

2.1. Synthesis of $Me_{1-x}Zn_xFe_2O_4$ nanoparticles

The magnetization of substituted ferrite nanoparticles synthesized by co-precipitation depends mostly on parameters such as reaction temperature, pH of the suspension, initial molar concentration, etc. [4]. Ultra fine particles of $Co_{1-x}Zn_xFe_2O_4$ with x varying from 0.1 to 0.5 were prepared by co-precipitating aqueous solutions of $CoCl_2$, $ZnSO_4$ and $FeCl_3$ mixtures, respectively, in alkaline medium. The mixed solution of $CoCl_2$, $ZnSO_4$ and $FeCl_3$ in their respective stoichiometry (50 ml of 0.5 M $CoCl_2$, 50 ml of 0.5 M $ZnSO_4$ and 100 ml of 1 M $FeCl_3$ in the case of $Co_{0.5}Zn_{0.5}Fe_2O_4$ and similarly for the other values of x) was prepared and kept at 80 °C. This mixture was added to the boiling solution of NaOH (0.64 M dissolved in 1300 ml of distilled water) within 10 s under constant stirring. Nanoferrites are formed by conversion of metal salts into hydroxides, which take place immediately, and transformation of hydroxides into ferrites. The solutions were maintained at 95 °C for 1 h. This duration was sufficient for the transformation of hydroxides into spinel ferrite (dehydration and atomic rearrangement involved in the conversion of intermediate hydroxide phase into ferrite) [4].

$Mn_{1-x}Zn_xFe_2O_4$ fine particles with x varying from 0.1 to 0.5 were also collected by following the same procedure, but aqueous solution of $MnCl_2$ was taken instead of $CoCl_2$. The pH of the co-precipitating agent (NaOH) was adjusted around 12 and precipitation was then carried out. This is due to the simultaneous formation of non-magnetic and paramagnetic particles at higher pH value $\geqslant 13$. The concentration of Mn^{2+} and Fe^{3+} deviates from their initial stoichiometry when higher pH is used for precipitation. But in the case of Co–Zn ferrite higher pH value did not affect the ferrite formation or the magnetization of the product.

2.2. Characterization

The particles were collected and separated using magnetic separation and washed several times with

distilled water followed by acetone and dried at room temperature. The particles were analysed using X-ray diffraction (XRD-Rigaku with Cu Kα radiation), high-resolution transmission electron microscopy (HRTEM-Hitachi HF 2000). The magnetization measurements were done at room temperature up to a maximum field of 10 kOe and the temperature dependence of magnetization in a field of 5 kOe were done using a vibrational sample magnetometer (VSM Tamakawa model TM-VSM1230-HHHS). The associated water content was estimated by thermo gravimetric analysis (TGA) by monitoring the weight of the sample when heated to a maximum of 700 °C (rate 5 °C/min) in an inert atmosphere (Mettler Toledo 851°). The water content was estimated from the weight difference measured at 25 and 700 °C. Estimation of Co^{2+}, Mn^{2+} and Zn^{2+} in the final product was carried out using double beam atomic absorption spectrometer (GBC-902). Flame type used was air acetylene and suitable lamps with wavelength 240.7, 279.5 and 213.9 nm for the estimation of cobalt, manganese and zinc, respectively were used. The Fe^{3+} ions were estimated by using UV–visible spectrophotometer (Shimadzu – UV-1601). The concentration of Fe^{3+} ion was estimated by measuring the absorbance at 510 nm using spectrophotometer. The reduction of iron was possible by addition of a mixture of sodium acetate and glacial acetic acid (Buffer), 5% hydroxylamine hydrochloride (reducing agent) and 0.25% O-Phenanthroline (complexing agent). The particles were dissolved using concentrated HCl and carefully diluted so that the dilution was well within the linear limit depending upon the sensitivity for the estimation of the respective cation [8].

3. Results and discussion

The final products after magnetic separation and subsequent washing and drying were used for the estimation of final cation concentrations. The exact amount of metal ions present in the final product was estimated after taking into consideration the estimated amount of associated water content from the TGA studies. The formation of ferrites was in accordance with their initial stoichiometry. The initial and final (estimated) cation concentrations of the prepared samples are given in Table 1. The ratio of $(Me^{2+})/(Fe^{3+})$ initially taken was 0.5 and the ratio obtained from the final product varied from 0.512 to 0.52 in the case of Co–Zn ferrite and from 0.5 to 0.51 in the case of Mn–Zn ferrites. Both the Co–Zn and Mn–Zn ferrites did not deviate (within the allowed experimental errors including estimation of water content, dilution etc.) from their initial stoichiometry and matched well with the initial degree of substitution when rounded to the first decimal. It is interesting to note that the initial and final Zn

Table 1
Initial and the estimated final cation concentrations of the prepared samples

Cation concentration						Samples with estimated cation
Co^{2+}/Mn^{2+}		Zn^{2+}		Fe^{3+}		
Initial	Final (estimated)	Initial	Final (estimated)	Initial	Final (estimated)	
0.9—Co	0.901	0.1	0.102	0.2	1.96	$Co_{0.901}Zn_{0.102}Fe_{1.96}O_4$
0.8—Co	0.81	0.2	0.204	0.2	1.98	$Co_{0.81}Zn_{0.204}Fe_{1.98}O_4$
0.7—Co	0.70	0.3	0.31	0.2	1.96	$Co_{0.70}Zn_{0.31}Fe_{1.96}O_4$
0.6—Co	0.61	0.4	0.41	0.2	1.96	$Co_{0.61}Zn_{0.41}Fe_{1.96}O_4$
0.5—Co	0.51	0.5	0.50	0.2	1.95	$Co_{0.51}Zn_{0.5}Fe_{1.95}O_4$
0.9—Mn	0.875	0.1	0.099	0.2	1.94	$Mn_{0.875}Zn_{0.099}Fe_{1.94}O_4$
0.8—Mn	0.789	0.2	0.21	0.2	1.96	$Mn_{0.789}Zn_{0.21}Fe_{1.96}O_4$
0.7—Mn	0.699	0.3	0.295	0.2	1.98	$Mn_{0.699}Zn_{0.295}Fe_{1.98}O_4$
0.6—Mn	0.591	0.4	0.399	0.2	1.96	$Mn_{0.591}Zn_{0.399}Fe_{1.96}O_4$
0.5—Mn	0.499	0.5	0.495	0.2	1.99	$Mn_{0.499}Zn_{0.495}Fe_{1.99}O_4$

concentration does not deviate and the preparation condition completely favors the formation of ferrites allowing us to study the effect of Zn substitution on the properties of the ferrites.

The particles collected were analyzed using XRD, and the diffraction pattern confirmed the formation of cubic ferrite phase for all the samples. The XRD pattern (Fig. 1a and b) indicates the formation of ferrite nanoparticles in both the cases of Co–Zn ferrites (Fig. 1a) and Mn–Zn ferrites (Fig. 1b). All the peaks in the diffraction pattern have been indexed and the refinement of the lattice parameter was done using Powder X software [9]. The average particle size for each composition has been calculated using the Debye–Scherrer formula. The peaks of (2 2 0), (3 1 1), (4 0 0), (5 1 1) and (4 4 0) have been deconvoluted to Lorentzian curves [10] using Peak Fit software for the determination of the average diameter (D_{XRD}) using full-width at half-maximum value (see Fig. 1a and b). The particle size estimated decreases with the increase in Zn concentration for Co–Zn as well as for Mn–Zn ferrites as shown in Fig. 2. Though all the samples were prepared under identical condition, the particle size was not the same for all concentrations of Zn. This was probably due to the reaction condition, which favored the formation of new nuclei preventing further growth of particles when the Zn concentration was increased. By altering the preparation condition and by making use of seeding technique, Jeyadevan et al. have produced a larger diameter particle with enhanced magnetization without altering the composition [4]. Hence, preparation condition serves as an effective means to have a control over the particle size. The preparation condition followed here gives rise to different rate of ferrite formation for different concentrations of Zn, favoring the variation of particle size.

The morphology of the particles formed was examined by direct observation via high-resolution transmission electron microscopy for all the collected particles. As an example, the micrographs of $Co_{0.5}Zn_{0.5}Fe_2O_4$ and $Mn_{0.5}Zn_{0.5}Fe_2O_4$ are given in Fig. 3a and b.

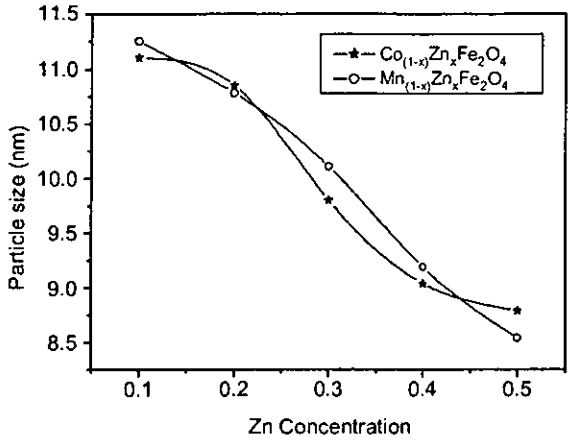

Fig. 2. Variation of particle size with increase in Zn concentration.

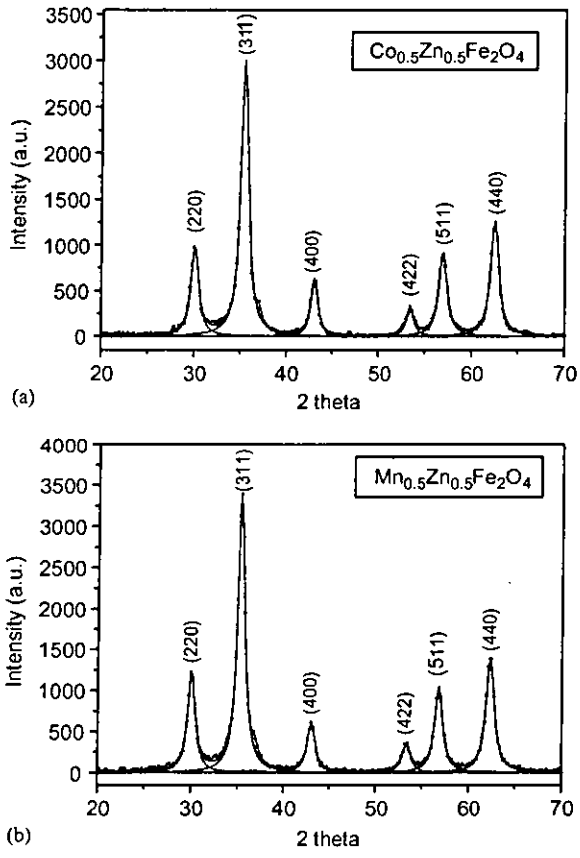

Fig. 1. The fitted XRD peaks of reflection (2 2 0), (3 1 1), (4 0 0), (5 1 1) and (4 4 0) for (a) $Co_{0.5}Zn_{0.5}Fe_2O_4$ and (b) $Mn_{0.5}Zn_{0.5}Fe_2O_4$ nanoparticles.

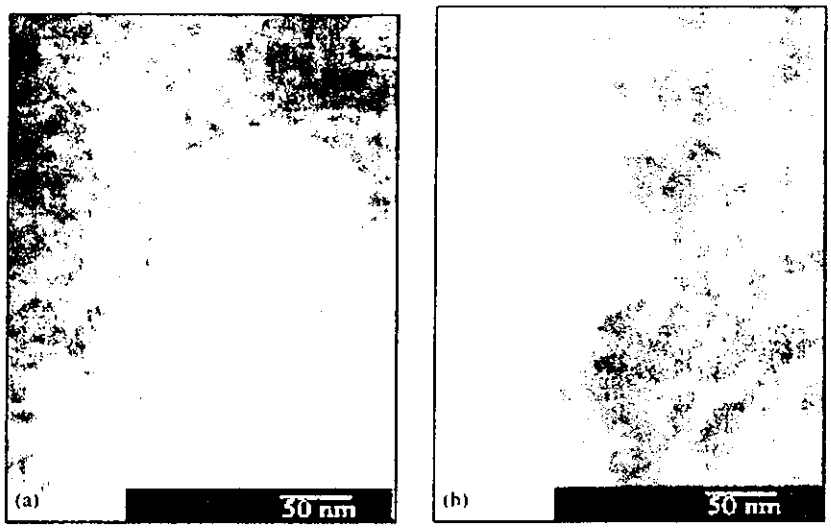

Fig. 3. Transmission electron micrograph of (a) $Co_{0.5}Zn_{0.5}Fe_2O_4$ and (b) $Mn_{0.5}Zn_{0.5}Fe_2O_4$.

Table 2
Summery of properties of $Co_{(1-x)}Zn_xFe_2O_4$ and $Mn_{(1-x)}Zn_xFe_2O_4$ nanoparticles

Samples with estimated cations	Magnetization measurements at 10 kOe			Estimated Curie temperature (°C)	Particle size D_{XRD} (nm)	Lattice parameter (Å)	Estimated associated water content Wt%
	M_s (emu/g)	M_r (emu/g)	H_c (Oe)				
$Co_{0.901}Zn_{0.102}Fe_{1.96}O_4$	54.1	10.6	223	415	11.1	8.390	10.9
$Co_{0.81}Zn_{0.204}Fe_{1.98}O_4$	50.7	4.84	76.2	373	10.9	8.387	11.55
$Co_{0.70}Zn_{0.31}Fe_{1.96}O_4$	48.8	2.35	33.5	352	9.8	8.385	12.19
$Co_{0.61}Zn_{0.41}Fe_{1.96}O_4$	42.8	0.798	11.6	285	9.0	8.383	14.43
$Co_{0.51}Zn_{0.5}Fe_{1.95}O_4$	39.6	0.499	9.77	267	8.8	8.356	16.65
$Mn_{0.875}Zn_{0.099}Fe_{1.94}O_4$	42.4	1.99	12.8	360	11.3	8.442	3.75
$Mn_{0.789}Zn_{0.21}Fe_{1.96}O_4$	48.1	1.45	9.02	—	10.8	8.440	9.04
$Mn_{0.699}Zn_{0.295}Fe_{1.98}O_4$	44.8	1.27	8.66	303	10.1	8.439	14.6
$Mn_{0.591}Zn_{0.399}Fe_{1.96}O_4$	35.1	0.717	8.58	196	9.2	8.436	14.75
$Mn_{0.499}Zn_{0.495}Fe_{1.99}O_4$	33.5	0.459	8.7	165	8.5	8.409	15.1

The lattice constant decreases to a very small extent with increase in the Zn concentration, but the difference is considerable only when the Zn concentration difference is large. This may arise when large number of Zn^{2+} ions having small ionic radii (0.74 Å) replace Mn^{2+} ions having large ionic radii (0.93 Å). In the case of Co–Zn ferrite both Co^{2+} and Zn^{2+} ions have small ionic radii and hence, the change in the lattice parameter is not well noticed (Table 2). The variation of lattice constant with increase in Zn concentration is shown in Fig. 4.

The specific magnetization (M_S), remanence (M_r) and coercivity (H_C) of the prepared powders were measured at room temperature in a maximum field of 10 kOe. Magnetic properties of Co–Zn and Mn–Zn ferrites are strongly dependent on the Zn concentration. The change in magnetic

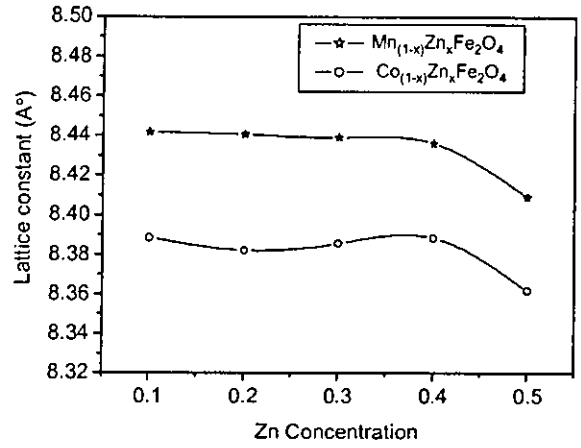

Fig. 4. Variation of lattice constant with increase in Zn concentration.

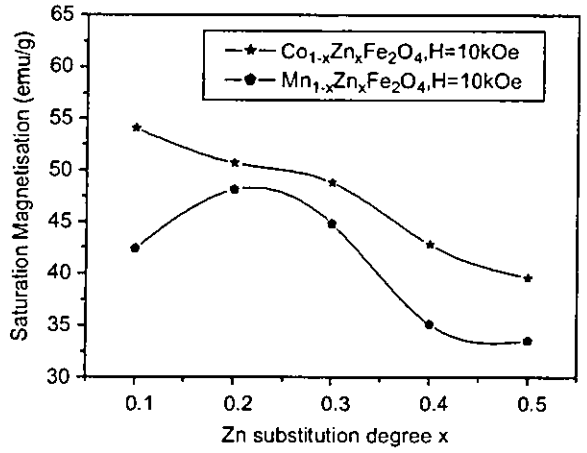

Fig. 5. Variation of saturation magnetization with Zn substitution at room temperature.

properties such as M_S, H_C and Curie temperature is due to the influence of the cationic stoichiometry and their occupancy in the specific sites as explained by Rath et al. [3]. In addition, formation of dead layer on the surface, existence of random canting of particle surface spins, non-saturation effects due to random distribution of particle size, deviation from the normal cation distribution etc., have been reported for the reduction in the magnetic properties of nanosized particles. The variation of saturation magnetization at room temperature with Zn substitution is shown in Fig. 5. The summary of properties of the particles derived from magnetic measurements, XRD and TGA are listed in Table 2.

Estimation of Curie temperature for the prepared samples is made by extrapolating the linear section of the temperature dependence of magnetization (M vs. T) to the temperature axis (Fig. 6a and b). A clear non-linear tail (from the extrapolated line to the region where the magnetization becomes zero) is seen for higher concentration of Zn substitution. A similar phenomenon called 'paraprocess' has been reported by Auzans et al. [2] for Mn–Zn ferrite nanoparticles for various Zn concentration and also by Chandana Rath et al.

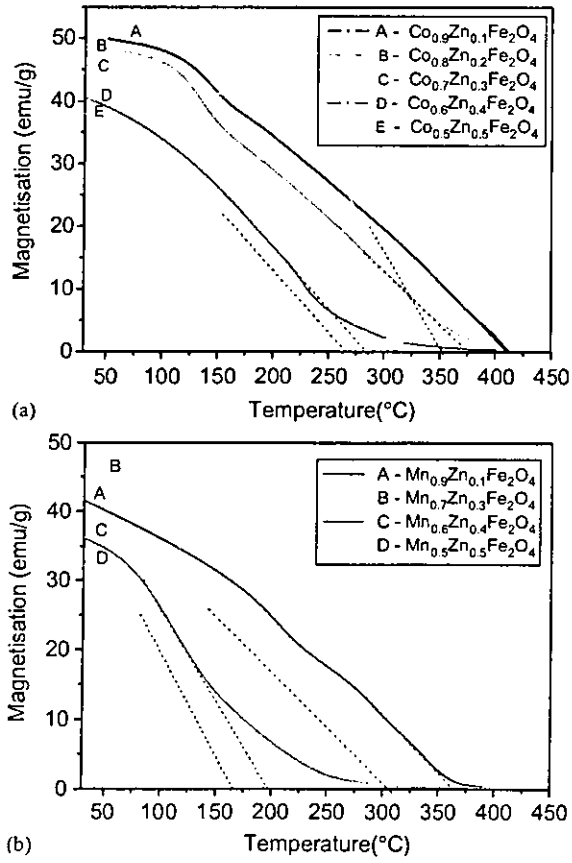

Fig. 6. Temperature dependence of magnetization of (a) $Co_{(1-x)}Zn_xFe_2O_4$ and (b) $Mn_{(1-x)}Zn_xFe_2O_4$.

Table 3
Thermomagnetic properties $Co_{(1-x)}Zn_xFe_2O_4$ and $Mn_{(1-x)}Zn_xFe_2O_4$ nanoparticles

Samples with estimated cations	Maximum value of thermomagnetic coefficient k_T (emu/gK)	Temperature at which k_T is maximum (°C)	Temperature range of $k_T \geqslant 0.2$
$Co_{0.901}Zn_{0.102}Fe_{1.96}O_4$	0.182	353	—
$Co_{0.81}Zn_{0.204}Fe_{1.98}O_4$	0.173	314	—
$Co_{0.70}Zn_{0.31}Fe_{1.96}O_4$	0.291	297	230–334
$Co_{0.61}Zn_{0.41}Fe_{1.96}O_4$	0.217	220	205–235
$Co_{0.51}Zn_{0.5}Fe_{1.95}O_4$	0.214	207	193–219
$Mn_{0.875}Zn_{0.099}Fe_{1.94}O_4$	0.177	204	—
$Mn_{0.699}Zn_{0.295}Fe_{1.98}O_4$	0.329	124	102–151
$Mn_{0.591}Zn_{0.399}Fe_{1.96}O_4$	0.265	111	83–145
$Mn_{0.499}Zn_{0.495}Fe_{1.99}O_4$	0.286	101	71–133

with the appearance of cusp along the non-linear tail [3]. From Table 2 it is clearly seen that the Curie temperature decreases with the addition of Zn. This is because of the replacement of more non-magnetic ions (Zn^{2+}) instead of Co^{2+} or Mn^{2+} in the A site [6].

Thermomagnetic coefficient k_T ($k_T = \Delta M/\Delta T$) is calculated from the first derivative of the temperature-dependent magnetization curve for each concentration. The maximum value of thermomagnetic coefficient and the temperature at which the maximum value is obtained are given in Table 3. The practical applications of ferrofluid is decided considering the stability of the fluid and the vapor pressure of the carrier liquid at the operating temperature [11]. Ferrofluid can be operated at a temperature around 150 °C without losing much of the stability. Ferrofluid having the maximum value of thermomagnetic coefficient within this temperature range can be utilized for energy conversion application. Particles whose value of $k_T \geqslant 0.2$ and the entire temperature range having this value of k_T are also given in Table 2. The value of k_T is $\geqslant 0.2$ only for $0.5 \geqslant x \geqslant 0.3$. In the case of $Co_{0.5}Zn_{0.5}Fe_2O_4$ the temperature range at which k_T is $\geqslant 0.2$ is around 200 °C, where as for $Mn_{0.5}Zn_{0.5}Fe_2O_4$ this temperature range is around 70 °C and hence can be effectively used for energy conversion applications. Simultaneous reduction in the Curie temperature and higher value of thermomagnetic coefficient shown by Mn–Zn ferrites (for $x = 0.5$ and 0.4) will enable us to prepare temperature sensitive ferrofluid for practical applications.

The percentage of Zn affects the associated water content, and the water content varies from 3.75% to 15.1% in the case of Mn–Zn ferrite and form 10% to 16.5% in the case of Co–Zn ferrite with corresponding increase in Zn substitution (Fig. 7). In both cases, the maximum percentage of water content (15% for $Mn_{0.5}Zn_{0.5}Fe_2O_4$ and 16.5% for $Co_{0.5}Zn_{0.5}Fe_2O_4$) estimated was for the higher substitution of Zn. This is because increase in the Zn concentration reduces the particle size and affects the rate of ferrite formation.

The water content was reduced to some extent only in the case of Co–Zn ferrites, in particular for the low substitution of Zn (showing 10% in our case) by slightly changing the preparation condition (when the precipitates were heated in the alkaline medium for 2 h instead of 1 h). This allowed even higher substitution of Zn ($x = 0.6$, etc.). The other properties due to this change in the preparation are not discussed here.

4. Conclusion

The preparation technique of nanoparticles has a definite impact on the control of particle size and alteration of magnetic properties. The estimated cations from the product are in comparison with the initial substitution degree, indicating that the

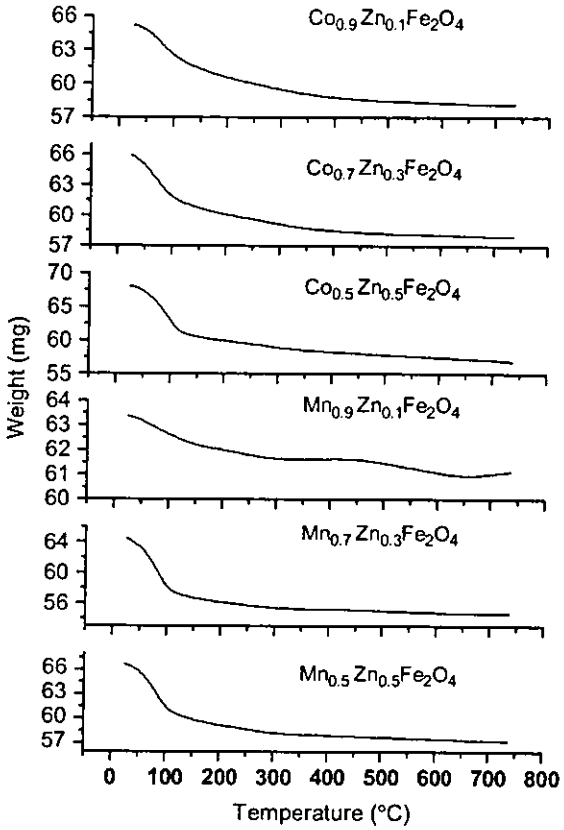

Fig. 7. Thermo gravimetric analysis of the prepared samples.

preparation procedure favors the formation of only ferrites. All the XRD peaks have been indexed and the lattice parameter have been estimated for each concentration. The particle size estimated showed a decreasing trend with the increase in the Zn concentration though the preparation condition was identical for all the samples. The Curie temperature and the temperature at which maximum value of thermomagnetic coefficient is observed decrease with the increase in Zn concentration. Thermomagnetic coefficient calculated for $Co_{(1-x)}Zn_xFe_2O_4$ and $Mn_{(1-x)}Zn_xFe_2O_4$ has maximum value of 0.2 when $x = 0.3-0.5$, but at different ranges of temperature for different values of Zn substitution. The Co–Zn ferrite particles can be used to prepare ferrofluids with higher magnetization. Mn–Zn ferrite particles with low Curie temperature and high value of thermomagnetic coefficient can be used for the preparation of temperature sensitive ferrofluid.

Acknowledgments

The authors are thankful the referees for their suggestions to bring the paper in the present form. The authors gratefully acknowledge Dr. Baldev Raj, Dr. Vasudeva Rao and Dr. S. V. Narasimhan of Indira Gandhi Centre for Atomic Research (IGCAR), Kalpakkam for extending some of the experimental facilities and to Dr. P.C. Scholten for his valuable suggestions. The support extended by Prof. K. Ethirajulu, Principal, Pondicherry Engineering College, Pondicherry deserves special mention.

References

[1] E. Auzans, D. Zins, E. Blums, R. Massart, J. Mater. Sci. 34 (1999) 1253.
[2] E. Auzans, D. Zins, E. Blums, R. Massart, Magn. Gidrodin. 36 (1) (1999) 78.
[3] C. Rath, S. Anand, R.P. Das, K.K. Sahu, S.D. Kulkarni, S.D. Date, N.C. Mishra, J. Appl. Phys. 91 (4) (2002) 2211.
[4] B. Jeyadevan, C.N. Chinnasamy, K. Shinoda, K. Tohji, J. Appl. Phys. 93 (10) (2003) 8450.
[5] K. Parekh, R.V. Upadhyay, R.V. Mehta, J. Appl. Phys. 88 (5) (2000) 2799.
[6] T. Upadhyay, R.V. Upadhyay, R.V. Mehta, Phys. Rev. B 55 (9) (1997) 5585.
[7] S. Dey, J. Ghose, Mater. Res. Bull. 38 (2003) 1653.
[8] G.H. Jeffery, J. Bassett, J. Mendham, R.C. Denney, Vogel's Textbook of Quantitative Chemical Analysis, Longman Group, UK, 1989, p. 691.
[9] C. Dong, J. Appl. Crystallogr. 32 (1999) 838.
[10] Y.I. Kim, D. Kim, C.S. Lee, Physica B 337 (2003) 42.
[11] P.C. Scholten, Chem. Eng. Comm. 67 (1988) 331.

Chemically Synthesized $L1_0$-Type FePt Nanoparticles and Nanoparticle Arrays via Template-Assisted Self-Assembly

Yuichi Sasaki, M. Mizuno, A. C. C. Yu, T. Miyauchi, D. Hasegawa, T. Ogawa, M. Takahashi, B. Jeyadevan, K. Tohji, K. Sato, and S. Hisano

Abstract—**Chemically ordered $L1_0$-type FePt nanoparticle agglomerates were synthesized directly by the co-reduction of Fe(III) and Pt(II) acetylacetonates in tetraethylene glycol at 300 °C in the absence of surfactants. These nanoparticles could be dispersed in n-hexane by coating with oleic acid and oleylamine. However, the dispersed particles exhibited only chemically disordered fcc phase and superparamagnetic behavior. The FePt nanoparticle film composed of dispersed particles and stabilized using amino-silane began to structurally transform to ordered $L1_0$ phase at 600 °C, which is lower compared to that prepared by the hot soap method. Rotational hysteresis loss measurement suggested that the ordering was incomplete at 600 °C and the nanoparticle film had the distribution of magnetocrystalline anisotropy field values. The FePt nanoparticle array was fabricated using the template-assisted self-assembly technique. To produce periodic dots on a substrate, positive-biased pulse voltage was applied to the substrate coated with octadecyltrichlorosilane monolayer by using a conducting cantilever used in a scanning probe microscope. This process induced electrochemical modification of $-CH_3$ groups into polar ones. The resulting template had well-aligned sub-100-nm dot arrays with sub-100-nm periodicity. The FePt nanoparticles were fixed on the patterned areas selectively.**

Index Terms—**Dispersion, electrochemical modification, FePt nanoparticle, $L1_0$ structure, magnetic anisotropy field, polycrystalline, polyol process, scanning probe lithography, template-assisted self-assembly.**

I. Introduction

THE $L1_0$-type alloys such as FePt and CoPt have great potential as the promising candidates for ultrahigh density recording media because of their high magnetocrystalline anisotropy (FePt: $K_u \sim 6.6 \times 10^7$ erg/cm^3, CoPt: $K_u \sim 4.9 \times 10^7$ erg/cm^3) [1]. Chemically synthesized FePt and CoPt nanoparticles have attracted much attention due to narrow size distribution as well as the dimensions with a few nanometer scale compared to those fabricated by the existing sputtering technique [2]–[9]. As-grown FePt and CoPt nanoparticles are mostly face-centered cubic (fcc) and show superparamagnetic behavior. To obtain ordered $L1_0$ structure, high temperature annealing is required. A self-assembled array of such particles shows well-aligned close-packed nanostructures on a substrate, however, each particle strongly coalesces during annealing [10], which results in undesirable increase in size and its distribution. Though doping with a third element (Ag) was effective in reducing the transformation temperature to 350 °C, it was impossible to prevent particles from coalescing completely [11]. We recently reported that $L1_0$-type FePt nanoparticles could be obtained directly in solution phase at 300 °C by using the "modified polyol process", which opened up the possibility for the fabrication of the ultrahigh density nanoparticle thin film media without heating process [12]. As the nanoparticle synthesis was carried out without using any stabilizers such as surfactants in solution, these particles agglomerated strongly so that the coating of the nanoparticles on a substrate was difficult. In the first part of this paper, the dispersion of the directly synthesized $L1_0$-type FePt nanoparticles in an organic solvent is investigated. The unique morphological and crystallographic characteristics are examined and compared with those synthesized by the hot-soap method [13]. The investigation of their magnetic properties focusing on the magnetic anisotropy is also discussed.

The ultimate goal in the development of ultrahigh density recording media is to store one bit per one magnetic unit. To achieve this, the establishment of periodic arrays is necessary. Various lithographic techniques have been used to fabricate the magnetic arrays [14], [15], however, periodic assembly of nanoparticles system with an extended area has not been accomplished. We demonstrated the application of amino-functional silane as a coupling layer for FePt nanoparticles dispersion, resulting in the formation of a monolayered film on a rigid substrate [16]. This fabrication method offered the possibility of a long-range array of the nanoparticles, however, no periodic array was formed. We have recently proposed the template assisted self-assembly technology, which incorporated scanning probe lithography as a promising tool for the establishment of such arrays [17]. In the second part of this paper, successful production of well-aligned FePt nanoparticles array is demonstrated.

II. Experiment

FePt nanoparticles with $L1_0$ structure were synthesized by co-reduction of Fe(III) and Pt(II) acetylacetonates in tetraethy-

Manuscript received August 20, 2004.

Y. Sasaki, M. Mizuno, A. C. C. Yu, and T. Miyauchi are with Sony Corporation Sendai Technology Center, Tagajo, Miyagi 985-0842, Japan (e-mail: Yuichi.Sasaki@jp.sony.com).

D. Hasegawa, T. Ogawa, and M. Takahashi are with Graduate School of Engineering, Tohoku University, Sendai, Miyagi 980-8579, Japan.

B. Jeyadevan and K. Tohji are with Graduate School of Environmental Studies, Tohoku University, Sendai, Miyagi 980-8579, Japan.

K. Sato and S. Hisano are with Dowa Mining Corporation, Honjo, Saitama 367-0002, Japan.

Digital Object Identifier 10.1109/TMAG.2004.838040

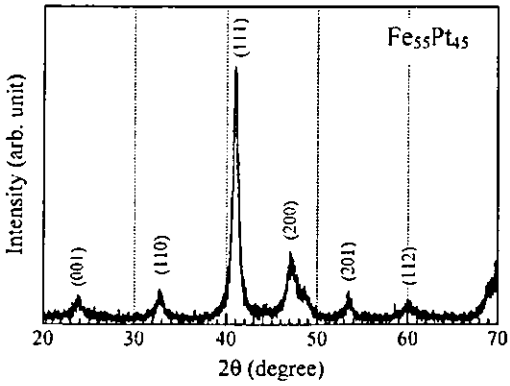

Fig. 1. Powder XRD pattern of FePt nanoparticles agglomerates synthesized by modified polyol process at 300 °C.

lene glycol (TEG) at 300 °C [9]. Contrary to the hot-soap method, the above method did not involve the stabilization of particles by surfactants. Thus the nanoparticles formed agglomerates and precipitated out. Dispersion of the nanoparticles in a nonpolar organic solvent was then carried out as follows: Oleic acid and oleylamine were injected into the solution after cooling down to room temperature, and a designated amount of n-hexane was added. The mixture was transferred into an airtight container, and agitated vigorously using a shaker. After several hours, the suspension separated into TEG and n-hexane phases. The n-hexane phase turned from colorless to dark brown, which is an indication of the presence of nanoparticles. Meanwhile, part of the nanoparticles remained at the interface between the two solvents. Thus this process was repeated to bring more particles into the n-hexane phase.

The FePt nanoparticles monolayered films were formed on a thermally oxidized Si wafer using a coupling layer of aminosilane [16]. Then, the monolayered film was annealed under a vacuum of 10^{-7} Torr at 600 °C for 30 min to evaluate the crystallographic features and magnetic properties.

The crystallographic textures and average grain sizes of the FePt nanoparticle monolayered films were investigated by in-plane X-ray diffraction (XRD) measurements with the X-ray incidence angle set at 0.25° from the plane. The in-plane XRD measurements were done using a RIGAKU ATX-G with Cu K_α (wavelength = 0.154 nm) radiation. On the other hand, the as-prepared and agglomerated FePt nanoperticles were examined using powder XRD. The particle morphology evaluation was carried out using high-resolution transmission electron microscopy (HR-TEM). Chemical compositions were determined by X-ray microanalysis (XMA). Magnetic properties were measured using a superconducting quantum interference device and high-sensitivity torque magnetometer.

III. Magnetic Properties and Crystallographic Structures of Directly Synthesized $L1_0$-Type FePt Nanoparticles

A. Morphology and Crystallographic Structures

Fig. 1 shows the powder XRD pattern of the as-prepared FePt nanoparticles before dispersion. Their average chemical composition analyzed using XMA was $Fe_{55}Pt_{45}$. The presence

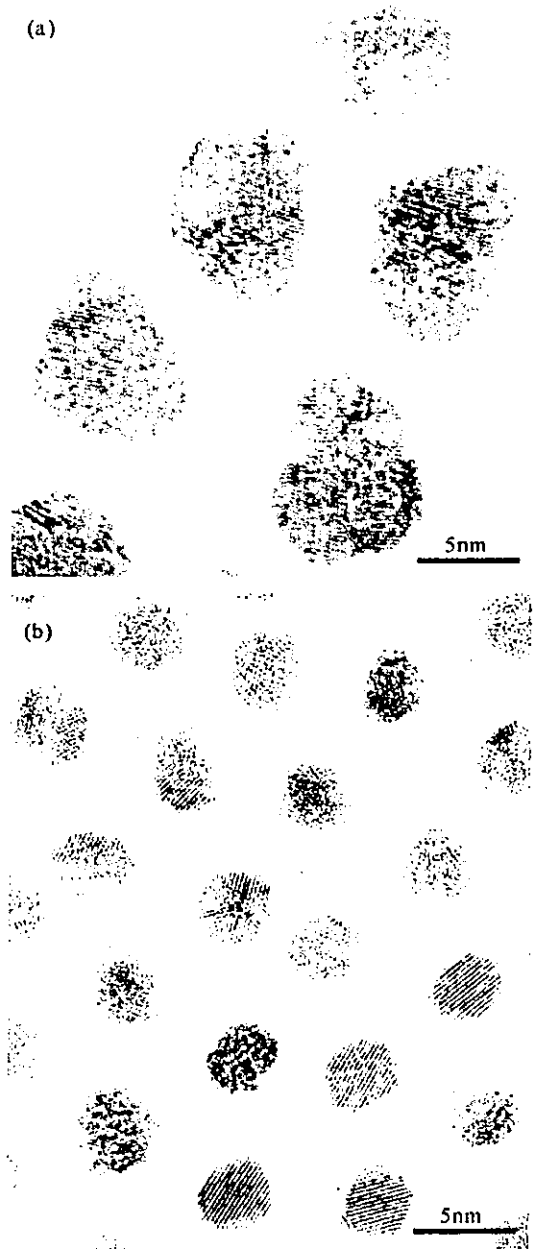

Fig. 2. HR-TEM images of the (a) dispersed portion of FePt nanoparticles synthesized by modified polyol process and (b) those prepared by the hot soap method.

of (001) and (110) superlattice reflections suggested the existence of $L1_0$ structure in the as-prepared FePt nanoparticles. The c/a ratio calculated using the (111) and (200) peaks was 0.972 and was slightly larger compared to that of the ideal bulk value which is only 0.964 [18]. This suggested the presence of partially ordered $L1_0$ phase. As previously reported [12], the sample consisted of agglomerates of nanoparticles with diameters ranging between 5 and 10 nm.

The HR-TEM image of the FePt nanoparticles dispersed in n-hexane is shown in Fig. 2(a). Mismatched lattice planes observed in almost all the particles confirmed the polycrystalline nature of the particles. This morphology was characteristic

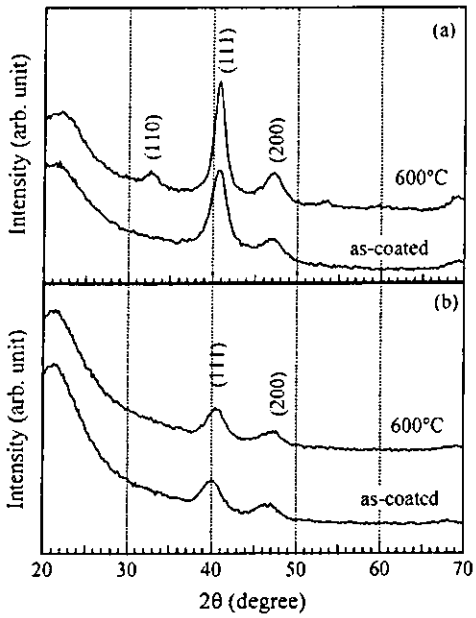

Fig. 3. In-plane XRD patterns for the as-coated and 600 °C annealed FePt nanoparticle monolayered films. (a) and (b) denote the dispersed portion of the nanoparticles synthesized by modified polyol process and those prepared by hot-soap method, respectively.

of the FePt nanoparticles synthesized by the modified polyol process (polycrystalline), and was different from that obtained by the hot-soap method (single crystalline) [13] as indicated in Fig. 2(b). The mean diameter of the particles was 7.6 nm with a standard deviation of 1.4 nm (18%). From XMA, the chemical composition of the dispersed FePt nanoparticles was found to be $Fe_{36}Pt_{64}$. The reason for this phenomenon is not clear yet, however, dissolution by oleic acid could be considered as a possible reason.

Fig. 3(a) shows the in-plane XRD patterns for the as-coated and 600 °C-annealed FePt monolayered films. The nanoparticles used here correspond to the dispersed portion of the particles synthesized by the modified polyol process. The profiles for the monolayered films of the FePt nanoparticles prepared by the hot-soap method are shown in Fig. 3(b) for comparison. Before annealing, only the chemically disordered fcc (111) and (200) peaks were observed for the film of the nanoparticles synthesized by the modified polyol process. This meant that the as-coated nanoparticles did not possess the $L1_0$ structure. The reason for this structural difference between the as-synthesized particles and the dispersed particles is unclear. A chemically ordered $L1_0$ (110) peak appeared for the 600 °C-annealed film of the nanoparticles produced by the modified polyol process and had a c/a ratio of 0.986 compared with 0.964 for the bulk [18]. Therefore, the sample has to be annealed at higher temperatures than 600 °C for more complete ordering. Conversely, no superlattice peak was confirmed in the XRD pattern for the film prepared using the particles synthesized by the hot-soap method even after annealing at 600 °C. From these results, we concluded that the structural transformation of the FePt nanoparticles synthesized by the modified polyol process occurred at lower temperatures than those by the hot-soap method. Besides the differences in the

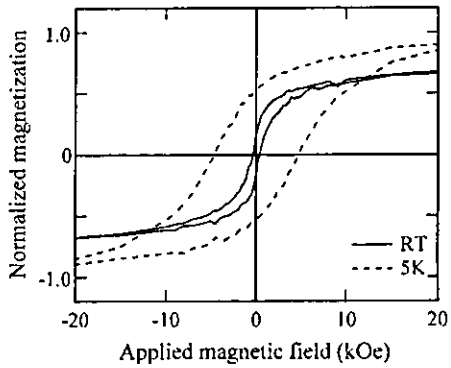

Fig. 4. In-plane hysteresis loops for the 600 °C annealed film of the dispersed FePt nanoparticles synthesized by modified polyol process measured at RT and 5 K.

reaction kinetics of the two preparation techniques, this phenomenon could be due to the following additional reasons, that is, the difference in morphological features of the nanoparticles prepared by both procedures and size dependence of ordering. As noted above, FePt nanoparticles synthesized by the modified polyol process were polycrystalline, while those by the hot-soap method were single crystalline. With a polycrystalline structure, ordering progresses due to interdiffusion of atoms within grains and at grain boundaries. The latter is expected to possess lower activation energy barrier, contributing to the reduction of the phase transformation temperature. Another possible reason is the dependence of phase transformation on the particle size. Recently, Takahashi *et al.* reported that smaller FePt particles were harder to chemically transform by applying the diffuse-interface theory [19]. The average grain diameter of the as-synthesized nanoparticles prepared by the hot-soap method, which was calculated by the Scherrer's equation using the full width at half maximum of the (111) peak, was 3.4 nm, which was slightly smaller than that by the modified polyol process of 4.1 nm. The former kept constant after annealing at 600 °C, while the latter increased up to 5.6 nm. Consequently, the ordering in nanoparticles prepared by the hot-soap method seems to be more difficult to progress. The grain diameter of the 600 °C-annealed nanoparticles was smaller than the average particle diameter measured by TEM observation, suggesting that the interparticle coalescence did not occur.

B. Magnetic Properties

The as-synthesized FePt nanoparticle agglomerates showed ferromagnetic behavior with a coercivity (H_c) of 2.2 kOe at room temperature (RT). On the other hand, the as-coated film of the dispersed nanoparticles showed superparamagnetic behavior at RT, which was consistent with the crystallographic fcc structure with low magnetic anisotropy. Fig. 4 shows in-plane hysteresis loops of the 600 °C-annealed film measured at RT and 5 K. It exhibited small H_c value of 290 Oe at RT, and 4.6 kOe at 5 K, which arises from the complicated contribution of incomplete ordering, slightly Pt-rich composition and small grain size of around 5 nm. The rotational hysteresis loss (W_r) for the 600 °C-annealed film of FePt nanoparticles synthesized by the modified polyol process is plotted as a function of the applied field up to 25 kOe in Fig. 5. As a reference, W_r curve